Conference on Modelling Fluid Flow (CMFF'22)
The 18th International Conference on Fluid Flow Technologies
Budapest, Hungary, August 30 -September 2, 2022

MACHINE LEARNING-BASED CLOSURE DEVELOPMENT FOR MODELING OF COHESIVE GAS-PARTICLE FLOWS

Josef TAUSENDSCHÖN, Mohammadsadegh SALEHI, Stefan RADL

[1] Institute of Process and Particle Engineering, Graz University of Technology. Corresponding Author E-mail: josef.tausendschoen@tugraz.at

ABSTRACT

Coarse-grid simulations of large-scale gas-solid flows using a filtered two-fluid model (fTFM) require appropriate sub-grid closure models to approximate unresolved physical phenomena. Such a sub-grid closure should be accurate enough to account for the effects of the inhomogeneous particle distribution. Several constitutive models are available in the literature for non-cohesive gas-solid flows, while they are not applicable for cohesive flows. Therefore, we aim to investigate the dependency of the drag force closure on the cohesion level, and integrate it into a drag correction concept based on machine learning (ML).

To do so, the results of fully-resolved CFD-DEM simulations of cohesive gas-particle flow are filtered with different filter sizes to develop a new drag closure. In detail, we simulated different systems by changing the cohesion level from cohesionless to highly cohesive, and the size of the systems, via coarse-graining. Afterwards, a dataset for the ML algorithm was created, and various markers were analyzed. Subsequently, a neural network-based drag correction model was created, trained, and tested with the identified markers. Finally, we benchmark the accuracy of the developed models for a range of cohesion levels.

Keywords: Multiphase Flows, Cohesive Gas-Particle Flows, Data-driven Modelling, Machine Learning

NOMENCLATURE

Bo	[-]	Bond number
Ca	[-]	Capillary number
$\underline{\underline{D}}$	[$1/s$]	Symmetric velocity gradient tensor
G	[$1/m^3$]	Filter kernel
$\underline{F}$	[N]	Force
Fr	[-]	Froude number
H_d	[-]	Drag correction function
H_{DNN}	[-]	DNN-based drag function
d	[m]	Particle diameter
f_{DNN}	[-]	Neural network function value
h	[-]	Activation function
h_{ij}^*	[-]	Dimensionless separation distance
$\underline{g}, g$	[m/s^2]	Gravitational acceleration
R	[m]	Particle radius
$\underline{r}$	[m]	Predefined spatial position
$\underline{n_{ij}}$	[-]	Unit normal vector betw. particles
p	[Pa]	Pressure
t	[s]	Time
$\underline{u}, \underline{v}$	[m/s]	Eulerian velocity vector
u, v	[m/s]	Individual component of the velocity vector
u_t	[m/s]	Terminal settling velocity
V_b^*	[-]	Dimensionless bridge volume
$\underline{w}$	[-]	Neural network weight vector
w_0	[-]	Neural network bias
$\underline{x}$	[m]	Spatial position on grid
α	[-]	Coarse-graining ratio
β	[kg/m^3s]	Drag coefficient
Δ_f	[m]	Fluid filter size
Δ_G	[m]	Fluid grid size
ϕ	[-]	Volume fraction
Λ	[-]	Liquid loading level
$\underline{\Phi_d}$	[N/m^3]	Interphase drag force
ρ	[kg/m^3]	Density
θ	[rad]	Contact angle of the liquid bridge
μ_l	[Pa s]	Liquid dynamic viscosity
σ	[N/m]	Surface tension
ψ	[-]	Neural network input
$\dot{\gamma}$	[$1/s$]	Shear rate
$\underline{\underline{\tau}}$	[kg/ms^2]	Phase stress tensor

Subscripts and Superscripts

cap	Capillary
DNN	Deep Neural Network
d	Drift
g	Gas
ref	Reference
P	Particle

s	Solid
sl	Slip
sgs	Sub-grid contribution
tot	Total
max	Maximum
min	Minimum
vis	Viscous
z	Z-direction
Eul	Eulerian
Micro	Microscopic
−	Filtered
~	Filtered and phase-weighted
*	Scaled dimensionless quantity

1. INTRODUCTION

Fine particles are widely used in various industrial sectors as these particles features high specific surface area, which increases the rate of heat and mass transfer [1]. In the petrochemical industry, small particles are used as reacting powders for pulverized coal combustion and gasification. Another example is fluid catalytic cracking process, in which fine particles are used as FCC catalysis [2]. In the pharmaceutical industry, active pharmaceutical ingredients (API) are typically fine, which can improve the dissolution and release rate in the body [3]. In the food industry, due to their high specific surface area, fine powders are desirable [4]. However, the effect of cohesive force on powder flowability becomes more important for fine powder, compared to coarse particles.

Powders with cohesive interactions force can be categorized from mildly cohesive to highly cohesive. The level of cohesion can be quantified based on the Bond number, which describes the ratio of cohesion forces to the gravitational force. In addition to van der Waals forces, particle can become cohesive due to presence of liquid bridge between the particles in the gas-solid systems. This cohesive force is associated with viscous and surface tension forces, quantified by a Bond and capillary number [5]–[7].

As these phenomena occur at a particle level, quantification of these forces is not easy to investigate through experimental approaches. However, detailed numerical simulation can be of significant help in analyzing the contribution of different forces in the strength of granule and powder flowability. Typically, two different approaches can be used in this regard: i) computational fluid dynamic (CFD) through Two-Fluid Method (TFM) approach[8]; ii) CFD coupled with Discrete Element Method (CFD-DEM)[9]. These approaches can be used in highly-resolved and un-resolved scales. However, the computational cost for the highly-resolved one is extremely high when simulating industrial scale systems. Therefore, application of filtered approaches as un-resolved method are desired especially for industrial-scale systems [10], [11].

Simulations of industrial-scale gas-particle flows based on the filtered Two-Fluid model (fTFM) approach, and therefore with coarse grids, depend critically on constitutive models that account for the effects of inhomogeneous structures at the sub-grid level [12]. The complexity of accounting for inhomogeneous structures increases when considering cohesive gas-particle flows [13].

Previously, an artificial neural network-based drag correction model was developed by Jiang et al. [14], [15] for non-cohesive gas-particle systems. However, the question persists if this model is useful for cohesive systems or not. Therefore, in our current contribution, we aim to analyze the influence of cohesion on the drag force closure and integrate it into a machine learning-based drag correction concept. Prior studies [16] identified the sub-grid drift velocity as the crucial quantity for modeling the filtered drag coefficient. Unfortunately, the drift velocity is unavailable in filtered simulations. To correctly reproduce mesoscale structures, and since the drift velocity is also computable, we start with detailed CFD-DEM-based (Computational Fluid Dynamics-Discrete Element Method) simulations, and filter them with different filter sizes to emulate quantities available in an fTFM simulation.

2. MODEL DESCRIPTION AND FILTERING PROCEDURE

We perform fully resolved CFD-DEM simulations of a 2D periodic box over a wide range of different setups. Subsequently, these simulations are filtered (i.e., spatially averaged) with different filter sizes. Coarse-grained CFD-DEM simulations are used to perform simulations with larger system sizes to limit the computational expense. The CFD part is realized within the framework of OpenFOAM® [17], and the DEM part is solved using LIGGGHTS® [18]. The coupling between these two tools is performed with CFDEM® [18].

2.1. Simulation setups

The fluid grid size Δ_G was chosen equal to three times the particle (or parcel in case of coarse-grained simulations) diameter. The domain size is 16 Δ_G x 2 Δ_G x 64 Δ_G in each respective regime. The coarse-graining ratio α is defined as the ratio of the parcel and primary particle diameter (simulations featuring primary particles are indicated by $\alpha = 1$). Coarse-grained parameters are scaled from the primary to the coarse system according to [19]. Cohesion results from liquid bridges between the particles. These liquid bridges are modelled after Wu et al. [20]. The liquid loading level Λ is unchanged over all cohesive simulations. The cohesion level is varied from cohesionless to highly cohesive. For detailed information about the used cohesion models see Append A. In Table 1 an overview of all performed simulation and their system parameters is given.

Table 1. Overview simulation regimes

	$\alpha = 1$	$\alpha = 3$	$\alpha = 5$
d_P [m]	150e-6	450e-6	7.5e-4
Δ_G [m]	450e-6	1.35e-3	2.25e-3
$\phi_{s,tot}$		0.10	
Domain size		16 Δ_G x 2 Δ_G x 64 Δ_G	
Primary particles	10,561	285,147	1,320,125
Parcels	-	10,561	10,561
Bo	0-20	0-100	0-100
Λ		0.001	
Ca		0.01	
Δ_f		3 Δ_G; 4 Δ_G; 5 Δ_G	

The calculated terminal settling velocity u_t for the primary particle is 0.8562 [m/s]. The reference time is $t_{ref} = u_t/g$ and therefore equal to 0.0873 [s]. In [19] comparable simulations needed 5 times t_{ref} to reach a statistical steady-state. Therefore, simulations are performed for nearly $30 \cdot t_{ref}$ in our present study. The time frame in which data was sampled ranged from $18 \cdot t_{ref}$ to $30 \cdot t_{ref}$, with sampling performed every 0.25 t_{ref}.

2.2 Filtering Procedure

Filtering operations are performed via CPPPO [21]. The filtered solid volume fraction is:

$$\bar{\phi}_s(\underline{x},t) = \iiint \phi_s(\underline{r},t)\, G(\underline{r}-\underline{x})\, d\underline{r} \qquad (1)$$

where $\underline{x}$ is the spatial position (any position in the grid), $\underline{r}$ is the predefined spatial position. The filtered gas volume fraction is then $\bar{\phi}_g = 1 - \bar{\phi}_s$.The box filter kernel or top-hat kernel $G(\underline{r}-\underline{x})$ is normalized so that $\iiint G(\underline{r}-\underline{x})\, d\underline{r} = 1$ and is defined by the fluid filter size Δ_f after:

$$G(\underline{r}-\underline{x}) = \begin{cases} \frac{1}{\Delta_f^3}, \text{if } |\underline{r}-\underline{x}| \le \frac{\Delta_f}{2} \\ 0, \text{otherwise} \end{cases} \qquad (2)$$

The filtered gas and solid velocity are then:

$$\underline{\tilde{u}_g} = \frac{1}{\bar{\phi}_g} \iiint G(\underline{r}-\underline{x})\, \phi_g(\underline{r},t)\, \underline{u_g}(\underline{r},t)\, d\underline{r} \qquad (3)$$

$$\underline{\tilde{u}_s} = \frac{1}{\bar{\phi}_s} \iiint G(\underline{r}-\underline{x})\, \phi_s(\underline{r},t)\, \underline{u_s}(\underline{r},t)\, d\underline{r} \qquad (4)$$

The filtered gas pressure is:

$$\bar{p}(\underline{x},t) = \iiint G(\underline{r}-\underline{x})\, p(\underline{r},t)\, d\underline{r} \qquad (5)$$

The mass and momentum conservation balances for filtered CFD-DEM equations of the gas and the solid phase can be found in Appendix B.

2.3. Closure for the interphase drag force

In our contribution we focus on the closure for the interphase drag and the mesoscale interphase force. The mesoscale interphase force is typically referred to as the sub-grid contribution of the interphase drag force, and denotated as $\underline{\Phi_{d,sgs}}$ in what follows. It is defined as the difference between the filtered Eulerian drag force $\underline{\bar{\Phi}_d}$ and the interphase drag force $\underline{\tilde{\Phi}_d}$ calculated based on the filtered slip velocity and the microscopic drag coefficient:

$$\begin{aligned} \underline{\Phi_{d,sgs}} &= \underline{\bar{\Phi}_d} - \underline{\tilde{\Phi}_d} \\ &= \overline{\beta^{Eul}\left(\underline{u_g} - \underline{u_s}\right)} \\ &\quad - \beta^{Micro}(\underline{\tilde{u}_g} - \underline{\tilde{u}_s}) \end{aligned} \qquad (6)$$

where β^{Eul} is the Eulerian drag coefficient. β^{Eul} is equal to the momentum exchange term in the performed CFD-DEM simulations. β^{Micro} is the drag coefficient evaluated based on filtered quantities using specific drag law, e.g. Beetstra et al. [22]. Analogously as in [16] the filtered Eulerian drag force (since not available in filtered simulations) is modelled by:

$$\begin{aligned} &\overline{\beta^{Eul}(\underline{u_g} - \underline{u_s})} \approx \beta^{Micro}(\underline{\tilde{u}_g} - \underline{\tilde{u}_s} + \underline{\tilde{v}_d}) \\ &= \overline{\beta^{Eul}}(\underline{\tilde{u}_g} - \underline{\tilde{u}_s}) \end{aligned} \qquad (7)$$

$\overline{\beta^{Eul}}$ is the filtered Eulerian drag coefficient. The sub-grid drift velocity $\underline{\tilde{v}_d}$ is defined by:

$$\underline{\tilde{v}_d} = \frac{\overline{\phi_s u_g}}{\bar{\phi}_s} - \underline{\tilde{u}_g} \qquad (8)$$

When rearranging Eqs. (6) and (7) one can describe the mesoscale interphase force by $\underline{\Phi_{d,sgs}} = \beta^{Micro}\, \underline{\tilde{v}_d}$. Using this definition and Eq. (6) we can finally model the filtered Eulerian drag force by:

$$\underline{\bar{\Phi}_d} = \underline{\tilde{\Phi}_d} \left(1 + \frac{\underline{\tilde{v}_d}}{\underline{\tilde{u}_g} - \underline{\tilde{u}_s}}\right) = \underline{\tilde{\Phi}_d}\, \underline{H_d} \qquad (9)$$

Where $\underline{H_d}$ is the so-called drag correction function, which must fulfil the following properties:

- $\underline{H_d} \to 1$ for sufficiently small filter sizes (i.e., "well-resolved" simulations).
- $\underline{H_d} \to 1$ in the dilute (i.e., a single particle sedimenting at its terminal speed) and dense limit (i.e., a closely-packed, hence homogeneous, particle suspension sedimenting at steady state).

If we rearrange Eqs. (7) and (9) on can see that the drag correction function can also be approximated by:

$$\frac{\bar{\beta}^{Eul}}{\beta^{Micro}} = 1 + \frac{\underline{\tilde{v}_d}}{\underline{\tilde{u}_g} - \underline{\tilde{u}_s}} = \underline{H_d} \qquad (10)$$

3. DEEP NEURAL NETWORK

Jiang et al. [14], [15] introduced the usage of a Deep Neural Network (DNN) instead of a correlation function to predict the sub-grid drift velocity and subsequently the drag correction function. We evolve this idea into cohesive systems. From this section on, note that the term 'scaled' is used in the manner typical of fTFM to describe dimensionless parameters. In contrast, the term 'normalized' describes the feature normalization (or "scaling") related to the DNN induced data preparation. In order to develop a correct and accurate DNN-based drag correction function, the target for the training, which of course also represents the prediction, must be defined first. Subsequently, the transformation of the prediction into the actual drag correction is specified.

3.1. Target scaling

Since dimensionless quantities are preferred, a direct prediction of the drift velocity is not provided and is unusual. Deep Neural Networks often require target normalization. This demands knowledge or a search of minimum or maximum values. The first one is often not available or ties the prediction to certain preconditions, the latter comes with high computational effort and is often not possible. Therefore, scaling the target with known and available system quantities is preferred. Preliminary tests showed that scaling and additional normalization of the target is not beneficial to the prediction quality. Subsequently, we simply scale the target and do not use any additional normalization. In the present contribution, we focus on the vertical drag correction, represented by the z-direction in our simulations. Thus, only the z-components of the velocities and the drag coefficients were used for our analysis.

Jiang et al. [14] scaled the drift velocity with the filtered solid volume fraction, creating $\bar{\phi}_s\,\tilde{v}_{d,z}$ as the target. In a preceding publication [15], they adapted the target to $\frac{\bar{\phi}_s\,\tilde{v}_{d,z}}{\phi_{s,max}\,u_t}$, making it dimensionless. Two other options appear to be possible dimensionless targets, (i) the drift velocity relative to the terminal settling velocity $\tilde{v}_{d,z}/u_t$, and (ii) the direct prediction of $\frac{\tilde{v}_{d,z}}{\tilde{u}_{g,z}-\tilde{u}_{s,z}}$ from Eq. (10). The first option gave worse results in preliminary tests, and the second option could lead to numerical problems. Finally, $\frac{\bar{\phi}_s\,\tilde{v}_{d,z}}{\phi_{s,max}\,u_t}$ is selected as the target. Using the example of a single-layer neural network, the prediction is then:

$$\frac{\bar{\phi}_s\,\tilde{v}_{d,z}}{\phi_{s,max}\,u_t} = f_{DNN} = h(\underline{w}^T\,\underline{\hat{\psi}} + w_0) \qquad (11)$$

Where $\underline{\hat{\psi}}$ is the normalized input of the neural network, and h is the activation function. $\underline{w}$ the weights of the layer and w_0 is the bias.

3.2. DNN-based drag correction function

To build the DNN-based drag function Eq. (11) is rearranged to:

$$H_{DNN} = \frac{\phi_{s,max}\,u_t}{\bar{\phi}_s(\tilde{u}_{g,z}-\tilde{u}_{s,z})}\,f_{DNN} \qquad (12)$$

In order to meet the requirements stated in Section 2.3, and to be consistent with Jiang et al. [15], H_{DNN} is corrected. If the filtered solid volume fraction $\bar{\phi}_s$ is outside the range of 0.01 to 0.55, the DNN-based drag function is set to zero. Within the specified range, the function value is used. The actual drag correction function is then:

$$H_{d,z} = 1 + \begin{cases} H_{DNN}\,, & 0.01 \le \bar{\phi}_s \le 0.55 \\ 0\,, & else \end{cases} \qquad (13)$$

3.3. Marker selection

All Eulerian quantities available in the simulation are in question as a marker or input quantity of the neural network. Also, system parameters like the Bond number or the filter length can be used. In addition, combinations of the available Eulerian quantities as well as markers calculable with small computational effort, e.g., the gradient of the pressure field, are applicable. Jiang et al. [15] used the dimensionless filter length Δ_f^* and the particle Reynolds number as system parameters. In our simulation dataset, the particle Reynolds number is not changing for a single sedimenting particle, hence it is replaced by the Bond number since it accounts for cohesion.

The relative slip velocity in z-direction $\tilde{u}_{sl,z}/u_t$, the filtered solid volume fraction relative to the maximum solid fraction $\bar{\phi}_s/\phi_{s,max}$, and the scaled gradient in the z-direction of the filtered gas pressure field $\overline{\nabla p_z^*}$ are used equally as in [15]. We add the scaled shear rate of the filtered slip velocity $\overline{\dot{\gamma}^*}$. The input vector $\underline{\psi}$ of the DNN is then defined like:

$$\underline{\psi} = \left(\Delta_f^*, \frac{\bar{\phi}_s}{\phi_{s,max}}, \frac{\tilde{u}_{sl,z}}{u_t}, \overline{\nabla p_z^*}, Bo, \overline{\dot{\gamma}^*}\right) \qquad (14)$$

For the detailed calculation of each marker, see Appendix C. All markers are scaled to be dimensionless. Since different orders of magnitudes are present within the input values and DNNs typically require normalization [23], markers are additionally normalized.

3.4. Marker normalization

The normalization process of the input vector follows:

$$\underline{\hat{\psi}} = (\underline{\psi} - \psi_{min})/(\psi_{max} - \psi_{min}) \qquad (15)$$

Where ψ_{min} and ψ_{max} are the minimum and maximum values of the respective marker. Before normalization, the available data is separated into training, validation, and testing data sets. The

respective min and max values are then searched in the training data and used to normalize (and denormalize) the validation and the testing data to avoid data leakage [24]. If a pre-trained neural network is used for prediction based on a new dataset, the applied normalization strategy offers two options: (i) normalize with min-and max-values based on the new input data, requiring a search over all values, or (ii) normalize with min-and max-values based on the model derivation. In the present contribution, we use the known values from the model derivation as its computationally less demanding.

3.5. Deep Neural Network Design

We use a DNN with three hidden layers, where the respective number of hidden nodes are 128, 64, and 32. Each hidden layer is followed by a Rectifying Linear Unit (ReLu) as the activation function. Regularization is ensured by adding a dropout layer after each hidden layer. The dropout rate for all is 0.05. Mini-batch training and Adam [25] are combined for optimizing the network. The minibatch size is 2048, equal to the number of CFD cells. The output layer has no (or a linear) activation function, typical for regression tasks [23]. Weights are initialized based on the "he uniform" distribution [26].

4. RESULTS

4.1. Filtering results

Before performing and filtering cohesive simulations, the filtering procedure is validated in the cohesionless setup with literature data from Ozel et al. [16]. Figure 1 shows the filtered Eulerian drag coefficient scaled by the microscopic drag coefficient over the relative drift velocity. This comparison only considers representative data, meaning that only $\overline{\beta_z^{Eul}}$ values higher or equal to zero are accepted. Eqs. (7) and (10) show then that -1 is the lower limit for the $\tilde{v}_{d,z}/\tilde{u}_{sl,z}$. From [16] no data over their the upper limit, defined where $\overline{\beta_z^{Eul}}$ and β_z^{Micro} are equal, is available. Within this range, the filtered data agrees very well with the literature data. One has to note that the literature data origins in 3D simulations, while the shown data is from pseudo-2D simulations.

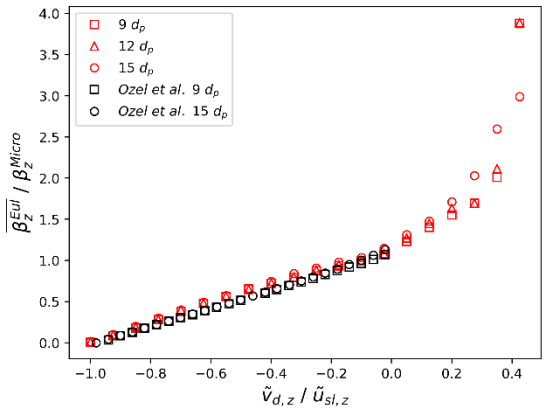

Figure 1. Scaled filtered Eulerian drag coefficient over the scaled drift velocity.

4.2. Prediction of the DNN

Figure 2 depicts an actual random snapshot of a simulation compared to the emulated one based on the DNN prediction. Here the actual target and output value of the DNN is shown (see Eq. (11)). As can be seen, regions of high negative values are qualitatively well predicted, while for positive values the prediction deviates.

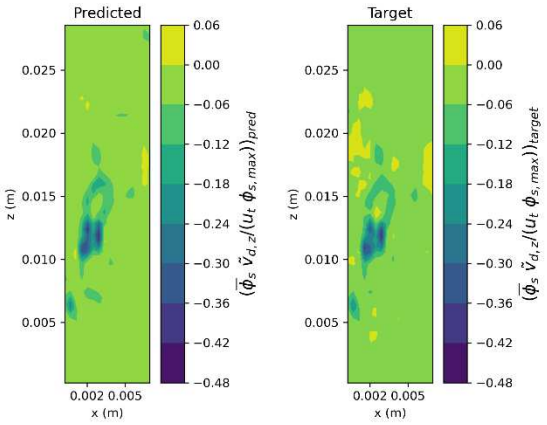

Figure 1. Contour plot of the scaled drift velocity. The left panel: DNN prediction. Right panel: target (ground truth).

For the quantitative perspective, Figure 3 shows a correlation plot for the DNN prediction and the target. The data points shown represent a single test dataset, while the displayed quality measures are from the entire test dataset. As can be seen, the coefficient of determination R^2 is equal to 0.9055, the means squared error is 2.613e-4, and the mean absolute error 8.997e-3.

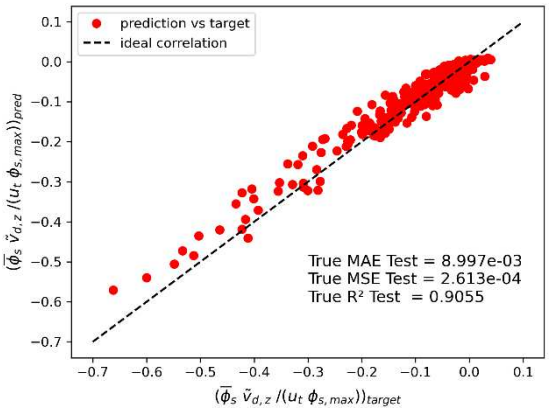

Figure 3. Correlation plot of the DNN prediction and the target for a single random test dataset.

Figure 4 shows the binned statistics of the DNN target over the filtered solid volume fraction. The shown data is based on the highly cohesive coarse-grained simulation with $\alpha = 5$ and $Bo = 90$. All filtered timesteps defined in Section 2.1 are considered. The prediction is depicted here separately for each filter length. As it can be seen, for the two smaller filter lengths the prediction is very accurate in medium to dense regions. In dilute regions, i.e. $\overline{\phi}_s$ smaller 0.1, the predictions of all filter lengths show higher deviations. The higher filter length leads to higher deviations over all solid volume fractions.

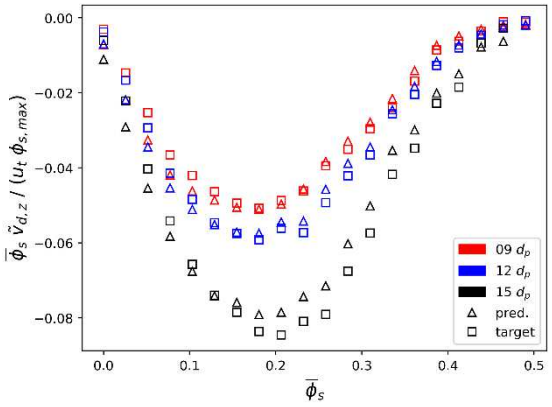

Figure 4. Target and prediction of the DNN binned with respect to the filtered solid volume fraction.

4.3. Drag correction function

After the detailed look on the DNN prediction in Figure 4, the focus here is shifted to the actual drag correction function. Based on the same highly cohesive data, Figure 5 shows the drag correction function over the filtered solid volume fraction. The aspect of Figure 4, that the highest deviations appear in the dilute regions is also found in Figure 5. In dilute regions, up to 0.1 solid volume fraction, a clear underprediction can be detected. Above and up to a filtered solid volume fraction of 0.40 the predictions are very close the target. In dense regions, the forecasts are sometimes very accurate, but also deviate in part. However, the prediction is more accurate than in dilute regions. The influence of the filter length is clearly visible.

In contrast to the direct prediction of the DNN shown in Figure 4 the big filter length does not lead to higher deviations.

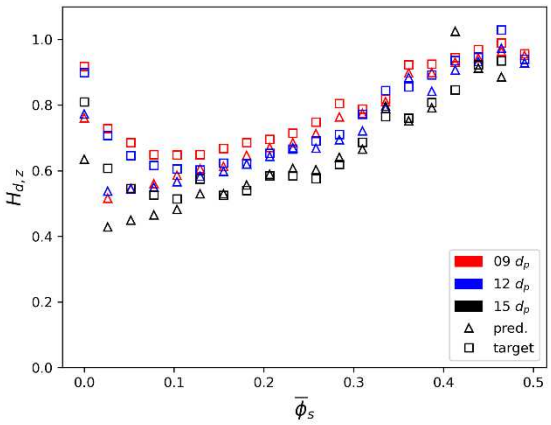

Figure 5. Drag correction function versus filtered solid volume fraction for different filter lengths.

5. SUMMARY

We performed fully-resolved CFD-DEM simulations in a 2D domain as the basis of a machine learning-based closure development for the modeling of cohesive gas-particle flows. These simulations were then filtered with different filter sizes to be able to develop such a drag closure for cohesive systems required for the fTFM approach. In detail, we simulated different systems by changing the cohesion level from cohesionless to highly cohesive, and the size of the systems, via coarse-graining. The filtering routine was successfully validated against literature data.

Then from the markers that are available in a basic fTFM simulation the ones with a high correlation to the defined target value, were selected. It has been shown that scaling the target to a dimensionless quantity is sufficient and that this avoids problems with respect to normalization. Nevertheless, that the input variables were also made dimensionless via scaling, an additional normalization is necessary. With the identified markers we then created, trained, and tested the neural network-based drag correction model.

The overall accuracy of the trained DNN is sufficient in terms of a robust drag correction prediction for a wide range of cohesion levels and system sizes. We additionally showed a detailed analysis of a highly cohesive simulation in a comparably large system. Three different ranges of particle volume fraction in terms of prediction

quality were observed. In dilute regions a clear underprediction was observed. For medium-dense areas, the predictions are very close to the target. In dense regions, the drag correction function varies between very accurate and less accurate. The influence of the filter length is clearly visible.

In our ongoing work the extension to 3D simulations is followed. These fully periodic systems will provide additional insights regarding drag correction. Specifically, investigations towards the anisotropy of the drag coefficient, and the associated corrections, can be expected from our 3D data.

APPENDIX A: COHESION MODELING

The cohesive force in the performed CFD-DEM simulations is the sum of the viscous and capillary force. The viscous force is described after Pitois et al. [27] by:

$$\underline{F_{vis}} = -\frac{3\,\pi}{2}\,\mu_l\,\frac{R}{h_{ij}^*}\,\underline{v_{n,0}}\,X_v^2\,\underline{n_{ij}} \tag{A.1}$$

$$X_v = 1 - \frac{1}{\sqrt{1+\frac{2\,V_b^*}{\pi\,h_{ij}^{*\,2}}}} \tag{A.2}$$

where μ_l is the liquid viscosity, R is the particle radius, $\underline{v_{n,0}}$ the impact velocity, $\underline{n_{ij}}$ the unit normal vector between the colliding particles and V_b^* the dimensionless bridge volume. The dimensionless separation h_{ij}^* is taken to be $h_{ij}^* = \max(h_{\varepsilon,eff}/R\,, h_{ij}^*)$, where $h_{\varepsilon,eff}$ is an effective roughness length of the particle. The capillary force model provided by Mikami et al. [28] is adopted in our present work:

$$\underline{F_{cap}} = \pi\,R\,\gamma\left[\exp\left(\mathrm{A}\,h_{ij}^* + \mathrm{B}\right) + \mathrm{C}\right]\underline{\mathrm{n}_{ij}} \tag{A.3}$$

$$A = -1.1\,(V_b^*)^{-0.53} \tag{A.4}$$

$$B = [-0.34\,\ln(V_b^*) - 0.96]\cdot\theta^2 - 0.019\,\ln(V_b^*) + 0.48 \tag{A.5}$$

$$C = 0.0042\,\ln(V_b^*) + 0.078 \tag{A.6}$$

θ is the contact angle of the liquid bridge. The dimensionless surface-surface separation distance is here defined as $h_{ij}^* = h_{ij}/R$. If particles overlap in a collision, the dimensionless separation distance is set to zero. The capillary number Ca is:

$$Ca = \frac{\mu_l\,u_t}{\sigma} \tag{A.7}$$

APPENDIX B: FILTERED EQUATIONS

For filtered CFD-DEM simulations the mass conservation balances for the gas and solid phase are:

$$\frac{\partial(\rho_g\bar{\phi}_g)}{\partial t} + \nabla\cdot\left(\rho_g\bar{\phi}_g\underline{\tilde{u}_g}\right) = 0 \tag{B.1}$$

$$\frac{\partial(\rho_s\bar{\phi}_s)}{\partial t} + \nabla\cdot\left(\rho_s\bar{\phi}_s\underline{\tilde{u}_s}\right) = 0 \tag{B.2}$$

The momentum conservation balance for the gas and solid phase are then:

$$\begin{aligned}&\frac{\partial(\rho_g\bar{\phi}_g\underline{\tilde{u}_g})}{\partial t} + \nabla\cdot\left(\rho_g\bar{\phi}_g\underline{\tilde{u}_g}\,\underline{\tilde{u}_g}\right)\\ &= -\bar{\phi}_g\nabla\bar{p} - \nabla\cdot(\rho_g\overline{\phi_g\underline{u_g''}\,\underline{u_g''}}) - \nabla\cdot\underline{\underline{\bar{\tau}_g}}\\ &+ \rho_g\bar{\phi}_g\underline{g} - \underline{\widetilde{\Phi}_d} - \overline{\phi_g'\nabla p'}\end{aligned} \tag{B.3}$$

$$\begin{aligned}&\frac{\partial\left(\rho_s\bar{\phi}_s\underline{\tilde{u}_s}\right)}{\partial t} + \nabla\cdot\left(\rho_s\bar{\phi}_s\underline{\tilde{u}_s}\,\underline{\tilde{u}_s}\right)\\ &= -\bar{\phi}_s\nabla\bar{p} - \nabla\bar{p}_s - \nabla\cdot(\rho_s\overline{\phi_s\underline{u_s'}\,\underline{u_s'}})\\ &- \nabla\cdot\underline{\underline{\bar{\tau}_s}} + \rho_s\bar{\phi}_s\underline{g} + \underline{\widetilde{\Phi}_d} - \overline{\phi_s'\nabla p'}\end{aligned} \tag{B.4}$$

Note that a single prime is used for the fluctuation from an algebraic average, e.g. $\underline{u_s'} = \underline{u_s} - \underline{\bar{u}_s}$ and a double prime for the fluctuation from a phase-weighted average, e.g. $\underline{u_g''} = \underline{u_g} - \underline{\tilde{u}_g}$.

APPENDIX C: CFD-DEM SIMULATION PARAMETERS

In Table C.1 all parameters of the performed CFD-DEM simulations, that are not included in Table 1, are summarized.

Table C.1. Simulation parameters

Particle density	2000 [kg/m³]
Gas Density	1.3 [kg/m³]
Gas Viscosity	1.44e-5 [Pa]
Young's modulus	4e6 [Pa]
DEM time step	1e-6 [s]
CFD time step	1e-5 [s]
Coeff. of restitution	0.4
Coeff. of friction	0.9
Coeff. of rolling friction	0.2

APPENDIX D: MARKER DEFINITIONS

The dimensionless filter length Δ_f^* is defined by:

$$\Delta_f^* = \frac{\Delta_f}{d_P\,Fr^{1/3}} \tag{D.1}$$

Where the Froude number Fr is ${u_t}^2/(g\,d_P)$. The scaled gradient of the gas pressure field in z-direction is:

$$\overline{\nabla p_z^*} = \frac{1}{\rho_s\,g}\frac{\partial\bar{p}}{\partial z} \tag{D.2}$$

The Bond number is:

$$Bo = \frac{6\,\sigma}{d_p^2\,g\,\rho_p} \tag{D.3}$$

Where σ is the surface tension. The dimensionless shear rate is:

$$\bar{\dot{\gamma}} = \frac{u_t}{g}\sqrt{2\cdot\underline{\underline{D}}:\underline{\underline{D}}} \tag{D.4}$$

Where $\underline{\underline{D}}$ is the symmetric velocity gradient tensor of the slip velocity. The scaled filtered slip velocity is

the difference between the filtered gas and filtered solid velocity:

$$\frac{\tilde{u}_{sl,z}}{u_t} = \frac{\tilde{u}_{g,z} - \tilde{u}_{s,z}}{u_t} \qquad \text{(D.5)}$$

REFERENCES

[1] F. Raganati, R. Chirone, and P. Ammendola, "Gas-solid fluidization of cohesive powders," *Chem. Eng. Res. Des.*, vol. 133, pp. 347–387, 2018.

[2] J. E. Galvin and S. Benyahia, "The Effect of Cohesive Forces on the Fluidization of Aeratable Powders," *AIChE J.*, vol. 60, no. 2, pp. 473–484, 2014.

[3] K. A. Mehta, G. S. Rekhi, and D. M. Parikh, *Handbook of Pharmaceutical Granulation Technology*. 2016.

[4] B. Cuq *et al.*, "Advances in Food Powder Agglomeration Engineering," vol. 69, J. B. T.-A. in F. and N. R. Henry, Ed. Academic Press, 2013, pp. 41–103.

[5] C. M. Boyce, A. Ozel, J. Kolehmainen, and S. Sundaresan, "Analysis of the Effect of Small Amounts of Liquid on Gas – Solid Fluidization Using CFD-DEM Simulations," vol. 63, no. 12, 2017.

[6] B. Buck, Y. Tang, N. G. Deen, H. Kuipers, and S. Heinrich, "Experimental investigation and force balance modelling of wet particle collisions," in *Particle Interactions 2018-Topical at the 8th World Congress on Particle Technology*, 2018, pp. 151–157.

[7] B. Buck and S. Heinrich, "Collision dynamics of wet particles: Comparison of literature models to new experiments," *Adv. Powder Technol.*, vol. 30, no. 12, pp. 3241–3252, 2019.

[8] M. Askarishahi, M. S. Salehi, and S. Radl, "Capability of the TFM Approach to Predict Fluidization of Cohesive Powders," *Ind. Eng. Chem. Res.*, vol. 61, no. 8, pp. 3186–3205, 2022.

[9] P. Grohn, D. Weis, U. Bröckel, S. Heinrich, and S. Antonyuk, "Contact models and dem simulation of micrometer-sized particles and agglomerates at static loading based on experimental characterization," in *Particles in Contact*, Springer, 2019, pp. 115–163.

[10] S. Radl and S. Sundaresan, "A drag model for filtered Euler–Lagrange simulations of clustered gas–particle suspensions," *Chem. Eng. Sci.*, vol. 117, pp. 416–425, 2014.

[11] M. Girardi, S. Radl, and S. Sundaresan, "Simulating wet gas–solid fluidized beds using coarse-grid CFD-DEM," *Chem. Eng. Sci.*, vol. 144, pp. 224–238, 2016.

[12] Y. Igci and S. Sundaresan, "Constitutive models for filtered two-fluid models of fluidized gas-particle flows," *Ind. Eng. Chem. Res.*, vol. 50, no. 23, pp. 13190–13201, 2011.

[13] M. H. Zhang, K. W. Chu, F. Wei, and A. B. Yu, "A CFD-DEM study of the cluster behavior in riser and downer reactors," *Powder Technol.*, vol. 184, no. 2, pp. 151–165, 2008.

[14] Y. Jiang, J. Kolehmainen, Y. Gu, Y. G. Kevrekidis, A. Ozel, and S. Sundaresan, "Neural-network-based filtered drag model for gas-particle flows," *Powder Technol.*, vol. 346, no. December, pp. 403–413, 2019.

[15] Y. Jiang, X. Chen, J. Kolehmainen, I. G. Kevrekidis, A. Ozel, and S. Sundaresan, "Development of data-driven filtered drag model for industrial-scale fluidized beds," *Chem. Eng. Sci.*, vol. 230, p. 116235, 2021.

[16] A. Ozel, Y. Gu, C. C. Milioli, J. Kolehmainen, and S. Sundaresan, "Towards filtered drag force model for non-cohesive and cohesive particle-gas flows," *Phys. Fluids*, vol. 29, no. 10, 2017.

[17] H. G. Weller, G. Tabor, H. Jasak, and C. Fureby, "A tensorial approach to computational continuum mechanics using object-oriented techniques," *Comput. Phys.*, vol. 12, no. 6, p. 620, 1998.

[18] C. Kloss, C. Goniva, A. Hager, S. Amberger, and S. Pirker, "Models, algorithms and validation for opensource DEM and CFD-DEM," *Prog. Comput. Fluid Dyn. An Int. J.*, vol. 12, no. 2/3, p. 140, 2012.

[19] J. Tausendschön, J. Kolehmainen, S. Sundaresan, and S. Radl, "Coarse graining Euler-Lagrange simulations of cohesive particle fluidization," *Powder Technol.*, vol. 364, pp. 167–182, 2020.

[20] M. Wu, J. G. Khinast, and S. Radl, "The Effect of Liquid Bridge Model Details on the Dynamics of Wet Fluidized Beds," *Am. Inst. Chem. Eng. J.*, vol. 62, no. 6, pp. 1877–1897, 2016.

[21] F. Municchi, C. Goniva, and S. Radl, "Highly efficient spatial data filtering in parallel using the opensource library CPPPO," *Comput. Phys. Commun.*, vol. 207, no. June, pp. 400–414, 2016.

[22] R. Beetstra, M. A. van der Hoef, and J. A. M. Kuipers, "Drag Force of Intermediate Reynolds Number Flow Past Mono- and

Bidisperse Arrays of Spheres," *AIChE J*, vol. 53, no. 2, pp. 489–501, 2007.

[23] J. Heaton, *Artficial Intelligence For Humans, Volume 3: Deep Learning and Neural Networks*. Heaton Research, Inc., 2015.

[24] S. Kaufman, S. Rosset, and C. Perlich, "Leakage in data mining: Formulation, detection, and avoidance," *Proc. ACM SIGKDD Int. Conf. Knowl. Discov. Data Min.*, pp. 556–563, 2011.

[25] D. P. Kingma and J. L. Ba, "Adam: A method for stochastic optimization," *3rd Int. Conf. Learn. Represent. ICLR 2015 - Conf. Track Proc.*, pp. 1–15, 2015.

[26] K. He, X. Zhang, S. Ren, and J. Sun, "Delving deep into rectifiers: Surpassing human-level performance on imagenet classification," *Proc. IEEE Int. Conf. Comput. Vis.*, vol. 2015 Inter, pp. 1026–1034, 2015.

[27] O. Pitois, P. Moucheront, and X. Chateau, "Liquid bridge between two moving spheres: An experimental study of viscosity effects," *J. Colloid Interface Sci.*, vol. 231, no. 1, pp. 26–31, 2000.

[28] T. Mikami, H. Kamiya, and M. Horio, "Numerical simulation of cohesive powder behavior in a fluidized bed," *Chem. Eng. Sci.*, vol. 53, no. 10, pp. 1927–1940, 1998.